Ocean Engineering 353 (2026) 124605

Contents lists available at ScienceDirect

Ocean Engineering

journal homepage: www.elsevier.com/locate/oceaneng

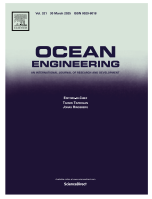

Research paper

Second-order wave excitation forces in WEC-Sim/MOST: Implementation, experimental validation, and code-to-code comparison

Davide Issoglio [a,*], Mohamed A. Shabara [b,1], Ermando Petracca [a,1], Francesco Niosi [a,1], Adam Keester [c,1], Massimo Sirigu [a,1], Giovanni Bracco [a,1]

[a] Marine Offshore Renewable Energy Lab (MOREnergy Lab), Department of Mechanical and Aerospace Engineering, Politecnico di Torino, Corso Duca degli Abruzzi 24, Torino, 10129, Italy
[b] National Laboratory of the Rockies (NLR), 15013 Denver West Parkway, Golden, CO, 80401, USA
[c] Sandia National Laboratories, 1515 Eubank Blvd SE, Albuquerque, NM, 87123, USA

ARTICLE INFO

Keywords:
Floating offshore wind turbines (FOWTs)
Second-order wave excitation forces
WEC-Sim/MOST
Experimental validation
Code-to-code comparison

ABSTRACT

Accurate prediction of second-order hydrodynamic loads is essential for floating bodies, including floating offshore wind turbines, wave energy converters, and hybrid wind–wave platforms. These nonlinear effects, arising from both sum- and difference-frequency forcing, are critical for capturing key response characteristics but remain challenging to model efficiently. In this work, we extend the open-source Wave Energy Converter Simulator / MATLAB for Offshore Simulation Tool by implementing second-order wave excitation forces, supporting both the full Quadratic Transfer Function formulation and the Newman approximation. The full Quadratic Transfer Function method is used for all code-to-code comparisons and experimental validation, while the Newman approximation is provided as a computationally lighter alternative. To benchmark the new capability, we perform a code-to-code comparison with OpenFAST and OrcaFlex. We then validate the enhanced model using wave-tank measurements of a 1:96 scale DeepCwind semi-submersible, showing that second-order effects are required to reproduce platform motions. The implementation employs a computationally efficient pre-computation strategy for second-order wave excitation forces, reducing simulation cost while maintaining engineering accuracy. Overall, this work advances the tool as an open-source and versatile tool for modelling floating offshore renewable-energy systems requiring second-order hydrodynamic fidelity.

1. Introduction

The global offshore wind sector has evolved from a niche market of shallow-water monopile turbines into a cornerstone of national energy efficiency roadmaps. Installed offshore capacity surpassed 75 GW in 2024, representing 11% of all new wind additions worldwide. Yet more than two-thirds of the planet's exploitable wind resource lies in waters deeper than 60–70 m, where fixed foundations become unfeasible or cost-prohibitive. Floating offshore wind turbines (FOWTs) offer a strategic pathway to unlock vast, high-quality wind regimes while minimising visual impact from shore. However, as floating platforms scale up, and as project developers push toward more exposed and energetic sites, the demand for predictive accuracy increases. In particular, platform motions and mooring loads are heavily influenced by low-frequency dynamics that arise from nonlinear wave–structure interactions.

FOWTs behave as compliant systems subject to multiple environmental excitations. Although incident linear wave energy is usually concentrated in the 5–20 s range, nonlinear hydrodynamic interactions produce secondary load cycles that fall outside this primary band. Specifically, difference-frequency interactions generate slowly varying loads that align closely with the natural periods of the platform's compliant modes (*surge*, *sway*, *yaw*), typically exceeding 100 s. These loads are driven by the "beating" phenomenon between wave components of slightly different frequencies, creating a wave envelope that excites large-amplitude resonant excursions, or "slow drift". Conversely, sum-frequency interactions produce high-frequency loads. While often secondary for catenary-moored semi-submersibles, these sum-frequency forces are critical for tension-leg platforms (TLPs) or stiff vertical-mooring systems, where they may excite springing-type responses, potentially inducing high-cycle fatigue in tendons or slender members Yang et al. (2021), Bureau Veritas (2019). Linear potential-flow theory is inherently blind to these nonlinear mechanisms. Consequently, relying solely on linear models leads to a systematic underestimation of extreme offsets, mooring fatigue loads, and resonant amplitudes, making the inclusion of Quadratic

* Corresponding author.
E-mail addresses: davide.issoglio@polito.it (D. Issoglio), akeeste@sandia.gov (A. Keester).
[1] These authors contributed equally to this work.

https://doi.org/10.1016/j.oceaneng.2026.124605
Received 12 December 2025; Received in revised form 30 January 2026; Accepted 7 February 2026
Available online 23 February 2026

Acronym Description

BEM	Boundary Element Method
BEM	Blade Element Momentum
CFD	Computational Fluid Dynamics
COG	Center of Gravity
DEL	Damage Equivalent Load
DOE	Department of Energy (USA)
DOF	Degrees Of Freedom
FD	Free Decay
FOWT	Floating Offshore Wind Turbine
IEC	International Electrotechnical Commission
MOST	MATLAB for Offshore Simulation Tool
MUR	Ministry of University and Research (Italy)
NLR	National Laboratory of the Rockies
NREL	National Renewable Energy Laboratory (USA)
PNRR	National Recovery and Resilience Plan (Italy)
PSD	Power Spectral Density
PTO	Power Take-Off
QTF	Quadratic Transfer Function
RF	Resonance Frequency band
TLP	Tension Leg Platform
WEC	Wave Energy Converter
WEC-Sim	Wave Energy Converter Simulator
WF	Wave Frequency band

Symbol Description

A_d	Drag area
A_{ij}	Frequency-dependent added mass matrix
A_∞	Infinite-frequency added mass matrix
$B(\omega)$	Radiation damping matrix
C_a	Added-mass coefficient
C_D	Quadratic drag coefficient
C_v	Linear viscous coefficient
$\mathbf{F}_{exc}$	Wave excitation force vector
$\mathbf{F}_{md}$	Mean drift force vector
F_t	Turbine thrust force
g	Gravitational acceleration
H_s	Significant wave height
m_0	Zero-order spectral moment
$\mathbf{M}$	Mass-inertia matrix
$\mathbf{n}$	Outward normal vector
p	Fluid pressure
T_p	Peak wave period
T_r	Resonance period
W_s	Wind speed
Φ	Velocity potential
ω	Wave frequency
ρ	Water density
ξ	Generalised displacement vector

Transfer Functions (QTFs) a fundamental requirement for reliable FOWT design.

As a result, there is growing recognition that mid-fidelity simulation tools must be extended to account for second-order wave excitation forces, especially when used for load assessment Robertson et al. (2020), control design Abbas et al. (2022b), Fontanella et al. (2021), or layout optimization Bai et al. (2025).

The most direct approach to obtaining second-order forces is by integrating the second-order pressure over the instantaneous wetted surface of the floater. In potential-flow theory, one expands the velocity potential Φ in a perturbation series $\Phi = \Phi^{(1)} + \Phi^{(2)} + \ldots$, and similarly the fluid pressure $p = p^{(0)} + p^{(1)} + p^{(2)} + \ldots$, where $p^{(2)}$ contains the quadratic products of the first-order terms. The second-order wave force is then obtained by the surface integral of $p^{(2)}$ (to leading order) on the body surface S in the equilibrium position.

$$\mathbf{F}^{(2)} = \oint_S p^{(2)}(\mathbf{x}, t)\, \mathbf{n}\, dS, \tag{1}$$

with $\mathbf{n} \in \mathbb{R}^3$ the outward normal. In the frequency domain, for two wave components of frequencies ω_i and ω_j, the second-order force amplitude can be obtained by integrating the products of the first-order potentials on S. The second-order force is expressed via QTFs as (for the ξ-direction):

$$H_\xi^-(\omega_i, \omega_j) = \rho \oint_S \left[\Phi^{(1)}_{\omega_i} \partial_n \Phi^{(1)}_{\omega_j} + \Phi^{(1)}_{\omega_j} \partial_n \Phi^{(1)}_{\omega_i}\right] n_\xi dS, \tag{2}$$

with $\Phi^{(1)}_\omega$ the first-order velocity potential at frequency ω, and ∂_n denoting the normal derivative, with analogous forms for sum-frequency QTF H_ξ^+. Implementations of this rigorous approach are available in standard industry panel codes like WAMIT, ANSYS AQWA, and WADAM. While accurate, this method demands fine discretization near waterlines and extensive computational resources, thus often necessitating careful numerical convergence studies, as recommended in DNVGL-RP-C205. To alleviate computational demands, Newman and Standing's Recent Developments (1987) approximations offer practical simplifications for difference-frequency forces when structure natural frequencies are substantially lower than incident wave frequencies. Newman WAMIT (2012) proposed approximating off-diagonal QTF terms by averaging diagonal elements:

$$H_\xi^-(\omega_i, \omega_j) \approx \frac{H_\xi^-(\omega_i, \omega_i) + H_\xi^-(\omega_j, \omega_j)}{2} \quad \text{for } |\omega_i - \omega_j| \ll 1. \tag{3}$$

This significantly reduces computational complexity; however, limitations arise when the QTF varies rapidly across frequencies, as seen in shallow-water or multicolumn structures Pinkster (1980), Cou (2013). In these scenarios, Newman's method tends to underestimate second-order loads, necessitating full-QTF implementation. The full-QTF method, considered the most precise within linear potential-flow theory, involves explicitly solving the second-order diffraction-radiation problem or indirect methods (Pinkster's integral corrections) without approximation. The total second-order force in irregular seas is then reconstructed as Pinkster (1980):

$$\begin{aligned} F_\xi^{(2)}(t) = &\sum_{i,j} H_\xi^-(\omega_i, \omega_j) A_i A_j \cos[(\omega_i - \omega_j)t + (\varepsilon_i - \varepsilon_j)] \\ &+ \sum_{i,j} H_\xi^+(\omega_i, \omega_j) A_i A_j \cos[(\omega_i + \omega_j)t + (\varepsilon_i + \varepsilon_j)], \end{aligned} \tag{4}$$

where $A_i \cos(\omega_i t + \varepsilon_i)$ represent individual wave components. The full-QTF approach ensures that all bispectral interactions are captured, thus accurately predicting critical phenomena such as slow-drift *surge* in semi-submersibles and high-frequency springing in TLPs. This method, extensively validated by model tests Cou (2013), is recommended explicitly by standards (e.g., International Electrotechnical Commission (IEC) 61400-3-2, DNVGL-RP-C205) for sensitive design scenarios where simplifications fail International Electrotechnical Commission (IEC), Dnvgl-rp-c205 (2017). Recent research explores slender-body methods to approximate second-order wave loads efficiently. Carmo and Hall Carmo and Hall (2025) introduced frequency domain slender-body techniques capable of predicting second-order drift forces accurately with drastically reduced computational effort, which is beneficial in preliminary analyses or optimization studies. Although less precise than full-QTF methods, slender-body approximations provide practical advantages when diffraction effects are minimal. In summary, accurate second-order wave load modeling is crucial for realistic offshore wind platform design, particularly to capture slow-drift motions influencing mooring system loads and structural integrity. The choice of method (full-QTF, Newman's approximation, or slender-body theory) should be guided by floater type, operational conditions, required accuracy, and computational budget, as dictated by prevailing industry standards and guidelines.

Table 1
Comparison of mid-fidelity FOWT simulation environments with respect to second-order wave-force modeling and numerical approaches.

Tool name	Physical domains	Second-order wave-force support	Experimental validation	Ref.
WEC-Sim/ MOST	Aero, potential/mid-fidelity hydro, mooring,	Newman/full-QTF (sum + diff. freq.), time-domain convolution with spectral truncation	Basin 2024 (this work)	WEC-Sim Documentation (2025)
OpenFAST	Aero, potential hydro, structural elasticity, mooring, control	Approximate (empirical diff. freq. via HydroDyn + optional QTF import)	OC3–OC6, OC5, OC6 Phase IV	Jonkman et al. (2024)
HAWC2	Aero, structural FE, linear hydro, quasi-static mooring	External input only (WAMIT QTF must be postprocessed)	LIFES50+, DeepCwind spar	Voltá i Roqueta et al. (2020), Larsen and Hansen (2025)
SIMA/ RIFLEX	Mooring and structural finite element method, hydro loads via Morison or Boundary Element Method	External postprocessing (with WAMIT or ANSYS AQWA QTF)	Hywind Demo, Statoil	Skaare et al. (2015)
OrcaFlex	Mooring (3D finite element method), hydrodynamic body loads, cable systems	External QTF import possible, mainly difference-frequency used	Kincardine, WindFloat, DeepCwind	Orcina (2023)

A broad suite of simulation tools has been developed in the scientific literature to model the coupled aero-hydro-servo-elastic dynamics of wind turbines. These efforts have resulted in tools with different modeling assumptions and fidelity levels. For instance, the WEC-Sim documentation WEC-Sim Documentation (2025) outlines the foundation for wave energy converter analysis, primarily focused on time-domain multibody dynamics. In the context of aeroelasticity, Larsen et al. Voltá i Roqueta et al. (2020) validated the Horizontal Axis Wind turbine simulation Code 2nd generation (HAWC2) for power production and load analysis. For coupled analysis including moorings, Skaare et al. Skaare et al. (2015) demonstrated the global response capabilities of the Simulation Workbench for Marine Applications (SIMA) against full-scale measurements from the Hywind Demo, the world's first full-scale floating wind turbine. Furthermore, commercial solutions such as OrcaFlex Orcina (2023) provide industry-standard modeling for moorings and hydrodynamic loads. These tools strike different balances between computational cost and physical resolution, as described in Table 1.

Despite substantial progress in second-order wave-force modeling, critical limitations persist in mid-fidelity FOWT tools. The simplistic adoption of Newman's approximation, which assumes constant phase and slowly varying QTF diagonals, suffices for horizontal slow drift in deep water, but significantly underestimates vertical-plane *heave* and *pitch* loading, especially for deep-draft or stiff platforms Simos et al. (2017), Zhang et al. (2020a). Experimental comparisons against full-QTF models confirm such underestimation, highlighting the inadequacy of simplified methods in FOWT design contexts Cou (2013), Simos et al. (2017).

Moreover, sum-frequency excitation is often neglected under the assumption that high-frequency structural modes are heavily damped. While valid for spar or semi-submersible platforms, this assumption becomes unsuitable for TLPs and tension-tether systems, where sum-frequency forces can excite tendon vibratory modes and contribute significantly to fatigue damage Bureau Veritas (2019).

There is also a pronounced lack of experimental validation under realistic irregular-wave conditions. Available validation studies are limited to short-duration monochromatic tests or use scaling to infer low frequency drift. Full-scale prototype data (e.g., WindFloat, Hywind) remain proprietary, leading to uncertainty in model reliability and conservative bias in design outcomes Mei and Xiong (2021), Stewart and Muskulus (2016). Without rigorous benchmarks, engineers favor simplifications, perpetuating the underestimation of second-order effects. Likewise, insufficient mesh and convergence controls in QTF panel methods amplify error risk, reducing confidence in pressure-integration outputs WAMIT (2012).

These limitations, ranging from the physical inaccuracy of simplified second-order load models to their limited computational tractability for large-scale design studies, highlight the need for a more accurate and efficient modeling strategy. In particular, the inability of Newman's approximation to capture vertical-plane response, the frequent exclusion of sum-frequency loads in TLP, the lack of validation, and the computational expense of full-QTF evaluations collectively restrict the use of second-order modeling in practical design and optimization workflows. This motivates the development of an efficient, fully time-domain implementation of second-order wave excitation forces within the Wave Energy Converter Simulator (WEC-Sim)/MATLAB for Offshore Simulation Tool (MOST) framework, in order to have a single tool with a structure that is easy for users to use, capable of performing efficient time-domain simulations of complex floating systems and able to capture all the main phenomena that influence their behavior, finding the appropriate balance between physical fidelity and computational cost. These are important factors, for example, in cases where it is necessary to explore many different designs or metocean conditions, a task that is difficult to perform using higher fidelity tools due to their high computational time costs. The principal novelty is the code comparison and the validation of results. The objective of the numerical–experimental comparison presented in this work is not to achieve pointwise agreement in amplitude, but rather to verify that the solver accurately reproduces the key spectral characteristics of the system response, namely, the rigid-body eigenfrequencies and the emergence of sum-frequency contributions. Detailed amplitude matching would require sea-state-specific tuning of viscous coefficients, which is beyond the present scope. Confidence in the baseline hydrodynamic module is supported by prior WEC-Sim validations. For example, Ruehl et al. Ruehl et al. (2016) verified the code against experimental data for point absorbers and oscillating surge converters. More recently, Repi and Diputra Repi and Diputra (2022) extended the validation to floating-point absorbers in irregular waves. Additionally, Huang et al. Huang et al. (2025) assessed the tool's performance for multi-body floating wave energy converters under actual sea states. No sea-state-specific tuning of Morison drag or empirical damping coefficients has been carried out; the coefficients adopted correspond to nominal design values derived from free-decay tests and remain fixed for all tests. Consequently, deviations in the absolute response amplitude are expected, particularly in severe sea states Wang et al. (2025). A similar modeling philosophy was followed by Cou (2013) and later by Zhang et al. (2020a), who demonstrated that, once Morison coefficients are left uncalibrated, numerical predictions systematically underestimate motion amplitude yet reproduce frequency content and phase relationships with high fidelity. This strategy keeps the numerical framework transferable to new sites and sea states without the need for ad hoc tuning.

The paper is organized as follows. Section 2 introduces the open-source WEC-Sim/MOST framework and outlines the new functionalities that enable the integrated design of FOWTs. Section 3 details the numerical implementation of second-order wave excitation forces within WEC-Sim. Section 4 describes the experimental campaign together with the numerical setup adopted for the code-to-code comparison, while Sections 5 and 6 present and discuss the results, highlighting the agreement among measurements, WEC-Sim/MOST, and established reference solvers.

2. WEC-Sim/MOST Tool description

WEC-Sim is an open-source toolbox for time-domain simulation of wave energy converters (WECs), and MOST extends WEC-Sim to FOWTs and hybrid wind-wave devices.

2.1. WEC-Sim

WEC-Sim is implemented in the MATLAB/Simulink environment and uses Simscape Multibody to model the six-degree-of-freedom (6-DOFs) dynamics of both rigid and flexible bodies, with or without hydrodynamic loading.

Wave forcing components are modeled using coefficients obtained from a frequency domain potential-flow boundary element method (BEM) solver. Common commercial examples include WAMIT, which is widely considered the industry standard for wave interaction analysis, and ANSYS AQWA, which integrates diffraction-radiation solving within a broader engineering suite. In the open-source domain, solvers such as NEMOH have been developed to provide accessible BEM capabilities, while the Python-based Capytaine offers a modern, scriptable linear potential flow solver. The BEM solutions are obtained by solving the Laplace equation for the velocity potential, which assumes that the flow is inviscid, incompressible, and irrotational. The equation of motion of each body is based on the Cummins equation Cummins (1962):

$$\begin{aligned}\mathbf{M}\ddot{\mathbf{X}}(t) =& \mathbf{F}_{\text{exc},1}(t) + \mathbf{F}_{\text{exc},2}(t) + \mathbf{F}_{\text{md}}(t) + \mathbf{F}_{\text{rad}}(t) \\ &+ \mathbf{F}_{\text{PTO}}(t) + \mathbf{F}_{\text{v}}(t) + \mathbf{F}_{\text{Mor}}(t) + \mathbf{F}_{\text{B}}(t) + \mathbf{F}_{\text{m}}(t),\end{aligned} \tag{5}$$

where $\mathbf{M} \in \mathbb{R}^{N_{\text{DOF}} \times N_{\text{DOF}}}$ is the mass–inertia system matrix, $\ddot{\mathbf{X}} \in \mathbb{R}^{N_{\text{DOF}} \times 1}$ is the translational/rotational acceleration vector, and $N_{\text{DOF}} \in \mathbb{N}$ is the number of generalized DOFs. Table 2 summarizes each load term.

The use of WEC-Sim requires specific external inputs:

- **Geometry files** ('.stl') for each floating body. *Note:* These files are for visualization and are mandatory only when nonlinear buoyancy or nonlinear Froude-Krylov forces are activated.
- **Hydrodynamic data** ('.h5'): Contains potential-flow theory coefficients and can be generated from BEM software results with WEC-Sim's BEM Input/Output (BEMIO) functions.
- **Input file** ('wecSimInputFile.m'): A MATLAB script that initializes and configures the simulation parameters.
- **Simulink model** ('.slx'): Created using WEC-Sim library blocks.

The WEC-Sim code structure (see Fig. 2) is object-oriented and organised around several core classes. Each class has a distinct function, as briefly summarized in Table 3.

The operational workflow of WEC-Sim can be summarized as follows:

1. **Geometry input**: Geometry file creation (for visualization and/or when nonlinear buoyancy or nonlinear Froude–Krylov forces are activated).
2. **Hydrodynamic data**: Use a BEM solver to compute hydrodynamic coefficients, then exploit BEMIO to convert the BEM outputs into an .h5 file format.
3. **Simulink model**: Build the WEC device model in Simulink using WEC-Sim library blocks.
4. **Input file**: In wecSimInputFile.m, instantiate and configure all necessary classes (simulation, waves, bodies, constraints, PTOs, moorings).
5. **Running the simulation**: Execute the simulation by running the command `wecSim` from the MATLAB command window inside the case directory.
6. **Postprocessing and analysis**: Analyze and visualize the simulation outputs (motions, forces, absorbed power) using built-in or user-defined postprocessing scripts.

Fig. 2 sketches the coupled aero-hydro-servo workflow. Green blocks are inherited from WEC-Sim; grey blocks are added by MOST.

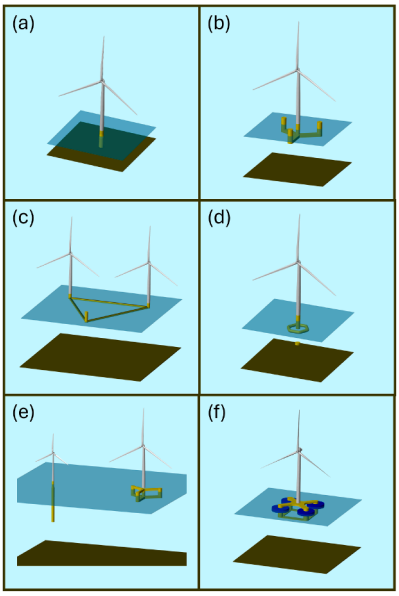

Fig. 1. Systems that can be implemented with WEC-Sim/MOST: (a) fixed platform, (b) single FOWT, (c) many turbines on the same platform, (d) pendulum-stabilized FOWT, (e) multiple FOWTs, and (f) hybrid platforms.

2.2. MOST

MOST introduces the wind turbine model, again using Simscape Multibody blocks, and the control of the latter, which can be chosen between the Baseline and ROSCO controllers (Hansen et al. (2005), Abbas et al. (2022a)). In addition, it adds the capability to simulate mooring systems with lookup tables built on a quasi-static nonlinear catenary model. It is now possible to perform simulations of a complete FOWT system as well as advanced configurations such as cases with multiple floating wind turbines with hydrodynamic coupling (Fig. 1(e)), hybrid wind-wave platforms (Fig. 1(f)), pendulum-stabilized platforms (Fig. 1(d)), and platforms with multiple turbines (Fig. 1(c)).

The classes introduced with MOST in the WEC-Sim framework are listed in Table 4.

MOST provides a suite of preprocessing functions to generate the files required to finalize the above-mentioned classes. The main operations performed are as follows:

- **Wind field generation**: Creation of turbulent wind field files using TurbSim by imposing some properties (average speed, turbulence intensity, time-varying elevation/azimuth angles, enabling yaw-misalignment studies within a single run, etc.).
- **Blade data and wind turbine properties**: Generation of global inertia properties from the basic geometric data of the turbine components (summarized in Fig. 3) and generation of lookup tables for the aerodynamic forces and torques at the root of the blades by providing as input the airfoil distribution and the lift and drag coefficients at different blade angles of attack. The lookup tables will have as input the local wind speed, rotor speed, and blade *pitch* angle and are computed through the blade element momentum (BEM) method, as described in Ning (2014) and Ning et al. (2026).
- **Control**: Generation of data used by the turbine control logic (whose actions are generator torque, blade *pitch* angle, and relative yaw angle between tower and nacelle) from previously defined turbine characteristics and certain user settings (such as natural frequency and damping factor of control loops, actuator limits, cut-in and cut-out wind speeds, etc.).

The functions introduced with MOST are effectively incorporated into the workflow of WEC-Sim, i.e., it is only necessary to make the ap-

Table 2
External forces in Eq. (5).

Force term	Formula and description
Linear wave excitation: $\mathbf{F}_{\text{exc},1}$	$\mathbf{F}_{\text{exc},1}(t) = \Re\left\{ R_f(t) \sum_{j=1}^{N} \mathbf{F}_{\text{exc}}(\omega_j, \theta) e^{i(\omega_j t + \phi_j)} \sqrt{2S(\omega_j)\Delta\omega_j} \right\}$ $R_f(t)$ is the ramp function; ω_j, ϕ_j are the discrete frequencies and phases; $S(\omega_j)$ is the wave energy spectrum; and $\mathbf{F}_{\text{exc}}(\omega_j, \theta)$ is the linear wave excitation transfer function, obtained via BEM. Setting $N = 1$ yields a regular wave.
Second-order wave excitation: $\mathbf{F}_{\text{exc},2}$	$\mathbf{F}_{\text{exc},2}(t) = \Re\left\{ \sum_{i=1}^{N}\sum_{j=1}^{N} A_i A_j X_{ij}^{+} e^{i(\omega_i+\omega_j)t} + \sum_{i=1}^{N}\sum_{j=1}^{N} A_i A_j^{*} X_{ij}^{-} e^{i(\omega_i-\omega_j)t} \right\}$ Sum and difference frequency second-order wave loads from QTF obtained via BEM (see Section 3).
Mean-drift: $\mathbf{F}_{\text{md}}$	$\mathbf{F}_{\text{md}}(t) = \left(\frac{H}{2}\right)^2 \mathbf{F}_{\text{md}}(\omega, \theta)$ Second-order mean drift force: H is the wave height; $\mathbf{F}_{\text{md}}(\omega, \theta)$ is the drift coefficient from BEM; steady component proportional to wave amplitude squared.
Radiation: $\mathbf{F}_{\text{rad}}$	$\mathbf{F}_{\text{rad}}(t) = -\mathbf{A}_{\infty}\ddot{\mathbf{X}}(t) - \int_0^t \mathbf{K}_{\text{rad}}(t-\tau)\dot{\mathbf{X}}(\tau)d\tau,$ $K_{\text{rad}}(t) = \frac{2}{\pi}\int_0^{\infty} \mathbf{B}(\omega)\cos(\omega t)d\omega$ $\mathbf{A}_{\infty}$ is the infinite-frequency added mass and $\mathbf{B}(\omega)$ is the radiation damping; both obtained via BEM. Optional computationally efficient state-space approximation.
Power take-off (PTO): $\mathbf{F}_{\text{PTO}}$	$\mathbf{F}_{\text{PTO}} = -K_{\text{PTO}}\Delta\mathbf{X} - C_{\text{PTO}}\Delta\dot{\mathbf{X}}$ K_{PTO} is the stiffness; C_{PTO} is damping; and $\Delta\mathbf{X}$ is the relative displacement. This is the linear spring-damper model (other models can be used).
Viscous damping: $\mathbf{F}_{\text{v}}$	$\mathbf{F}_{\text{v}} = -C_v\dot{\mathbf{X}} - \frac{1}{2}\rho C_D A_d \dot{\mathbf{X}}\lvert\dot{\mathbf{X}}\rvert$ C_v is the linear viscous coefficient; C_D is the quadratic drag coefficient; ρ is the fluid density; and A_d is the drag area.
Morison element: $\mathbf{F}_{\text{Mor}}$	$\mathbf{F}_{\text{Mor}} = \rho V\dot{\mathbf{u}} + \rho V C_a(\dot{\mathbf{u}} - \ddot{\mathbf{X}}) + \frac{1}{2}\rho C_D A_d(\mathbf{u} - \dot{\mathbf{X}})\lvert\mathbf{u} - \dot{\mathbf{X}}\rvert$ V is the displaced volume; $\mathbf{u}$ is the local fluid velocity; C_a is the added-mass coefficient; C_D is the drag coefficient; and A_d is the drag area Morison et al. (1950).
Buoyancy: $\mathbf{F}_{\text{B}}$	$\mathbf{F}_{\text{B}} = -mg + \rho V\vec{g} - \rho V\vec{g} \times (C_g - C_B) + K_{hs}X$ Buoyancy restoring force/torque vector, composed of gravitational force, buoyancy force, torque due to displacement between the center of gravity ($\mathbf{C}_g$) and the center of buoyancy ($\mathbf{C}_B$) at rest, plus a contribution from the hydrostatic stiffness matrix $\mathbf{K}_{\text{hs}}$, which acts as a linear restoring force/torque toward equilibrium position.
Mooring: $\mathbf{F}_{\text{m}}$	Mooring loads computed via linear stiffness and damping matrices, nonlinear quasi-static model lookup tables, or lumped-mass dynamic model (MoorDyn Moo (2020)).

Table 3
WEC-Sim (legacy) classes.

Class Name	Description
`simulationClass`	Defines global simulation settings: environment variables, time step, start and end times, solver options, etc.
`waveClass`	Specifies incident wave conditions: type (noWave, regular, irregular, spectrumImport, elevationImport), wave height, period, spectrum type, directional spreading.
`bodyClass`	Represents each body. It contains the mass and hydrodynamic properties of each body, defined by hydrodynamic data from the *.h5 file. The corresponding body block uses the hydrodynamic data and wave class to calculate all relevant forces on the body and solve for its resultant motion. At a high level, the body class interacts with the rest of WEC-Sim as shown in the diagram below.
`constraintClass`	Defines mechanical constraints: types of joints (e.g., fixed, revolute) between bodies or to the seabed.
`ptoClass`	Models PTO systems: linear spring-damper models, hydraulic or mechanical PTOs. Computes power absorption.
`mooringClass`	Represents the mooring system: modeled either with a linear stiffness matrix, lookup tables, or dynamic lumped-mass models.
`cableClass`	Includes external cable model for bodies' connection to each other and/or with seabed.

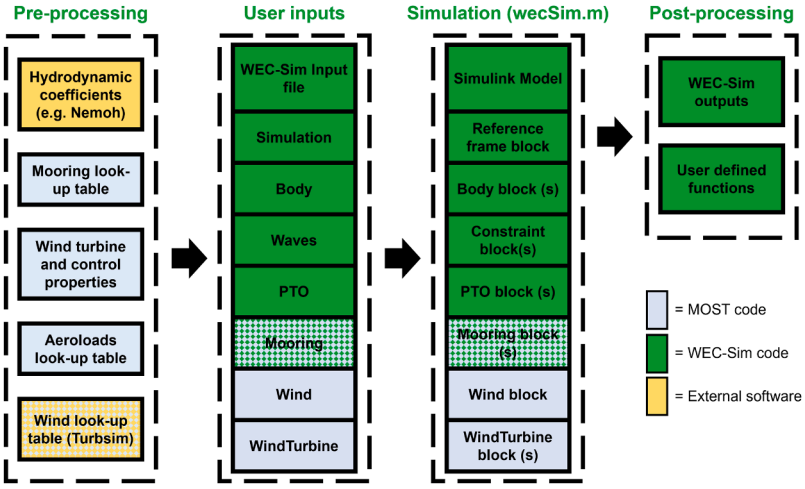

Fig. 2. WEC-Sim workflow including MOST features.

Table 4
WEC-Sim classes introduced with MOST.

Class Name	Description
`windClass`	Generation of the wind field, which can be constant (constant in space, with the capability of varying in modulus and direction over time) or turbulent (wind field generated using external tool TurbSim)
`windTurbineClass`	Definition of geometric and inertial properties of wind turbine components and its control logic

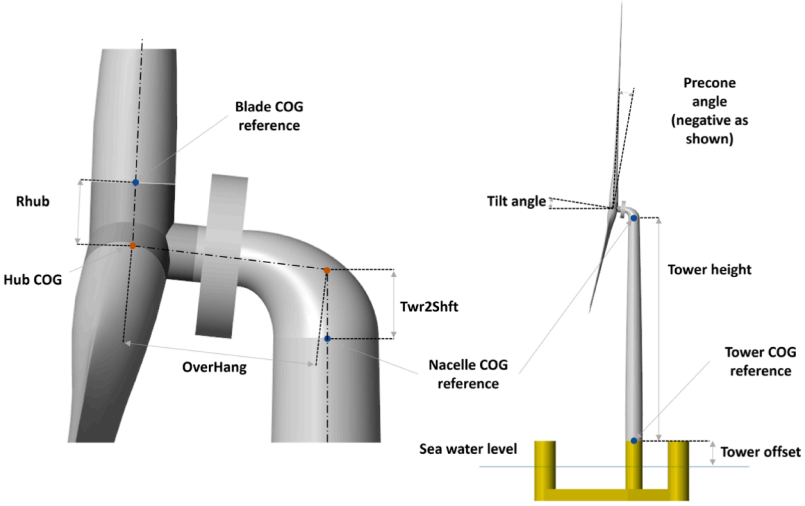

Fig. 3. Wind turbine geometric inputs.

propriate changes to points 3 and 4 described above. Specifically, there is a Simulink library (MOST_Lib.slx) with the wind turbine model that can be easily integrated with the libraries already present, and it is sufficient to initialize and define the additional classes in the same main input file (wecSimInputFile.m).

3. Implementation of second-order forces in WEC-Sim

WEC-Sim's implementation of the QTFs mirrors that of OpenFAST Jonkman et al. (2024) and has the ability to use either the full-QTF representation, implemented in the frequency domain, or the Standing approximation Recent Developments (1987). The Standing approximation is a variation of the Newman approximation for calculating the slowly varying wave-force component. Unlike the traditional Newman approach, the Standing approximation does not require applying a low-pass filter, thereby simplifying the processing workflow.

In this paper, we do not investigate the implementation of the Standing approximation in WEC-Sim. Instead, our focus is on the validation of the full-QTFs, which provide the complete second-order wave-loading representation without relying on approximations or filtering assumptions. The QTF force can be split into slowly varying (drift), $F^{(-)}_{exc,2}(t)$, and fast-varying (sum-frequency) $F^{(+)}_{exc,2}(t)$ components:

$$\mathbf{F}_{exc,2}(t) = \mathbf{F}^{(-)}_{exc,2}(t) + \mathbf{F}^{(+)}_{exc,2}(t). \tag{6}$$

WEC-Sim's full-QTF implementation calculates the second-order forces in the frequency domain and applies an inverse fast Fourier transform to obtain the force time series in the preprocessing step. In the full-QTF implementation, the slow- and fast-varying components (for each DOF) can be expressed as:

$$\mathbf{F}_{exc,2}(t) = \mathrm{Re}\left\{ \sum_{i=1}^{N}\sum_{j=1}^{N} (A_i A_j X^{+}_{ij} e^{\hat{i}(\omega_i+\omega_j)t} + A_i A^{*}_{j} X^{-}_{ij} e^{\hat{i}(\omega_i-\omega_j)t} \right\} \tag{7}$$

$$\mathbf{F}^{(+)}_{exc,2}(t) = \mathrm{Re}\left\{ \sum_{i=1}^{N} \sum_{j=1}^{N} A_i A_j X^{+}_{ij} e^{\hat{\imath}(\omega_i+\omega_j)t} \right\} \tag{8}$$

$$\mathbf{F}^{(-)}_{exc,2}(t) = \mathrm{Re}\left\{ \sum_{i=1}^{N} \sum_{j=1}^{N} A_i A^{*}_j X^{-}_{ij} e^{\hat{\imath}(\omega_i-\omega_j)t} \right\}, \tag{9}$$

where * refers to the conjugate complex, $\hat{\imath} = \sqrt{-1}$, $A_i = A(\omega_i) \in \mathbb{C}^N$ is the complex amplitude for the i^{th} wave component, and $X_{ij} = X(\omega_i, \omega_j) \in \mathbb{C}^{N\times N}$ is the frequency domain excitation force coefficient due to the interaction between the i^{th} wave frequency component and the j^{th} wave frequency component. It is important to note that the second-order frequency domain excitation coefficients have the following properties:

$$X^{+}(\omega_i, \omega_j) = X^{+}(\omega_j, \omega_i) \tag{10}$$

$$X^{-}(\omega_i, \omega_j) = X^{-*}_{i}(\omega_j, \omega_i). \tag{11}$$

Solving Eq. (7) directly involves evaluating a double inverse Fourier transform, resulting in a computational complexity of order $\mathcal{O}(N^2)$. To reduce the computational cost, Duarte et al. Duarte et al. (2014) exploited the symmetry properties described in Eqs. (10) and (11). By partitioning the double summation into three distinct cases, $(i = j)$, $(i > j)$, and $(i < j)$, and introducing the change of variables $\mu^- = j - i$ and $\mu^+ = j + i$, Eq. (8) can be reformulated into a more computationally efficient form:

$$F^{(+)}_{exc,2}(t) = \mathrm{Re}\left\{ \sum_{i=1}^{N} A_i A_i X^{+}_{ij} e^{\hat{\imath}(2\omega_i t)} + 2 \sum_{\mu^+=2}^{2N} H_{\mu^+} e^{\hat{\imath}(\omega_{\mu^+}-1)t} \right\}, \tag{12}$$

where H_{μ^+} is a piecewise function such that:

$$H_{\mu^+} = \begin{cases} \sum_{i=1}^{\lfloor(\mu^+-1)/2\rfloor} A_i A_{\mu^+-i} X^{+}(\omega_i, \omega_{\mu^+-i}) & \mu^+ = 2, 3, \ldots, N+1 \\ \sum_{i=\mu^+-N}^{\lfloor(\mu^+-1)/2\rfloor} A_i A_{\mu^+-i} X^{+}(\omega_i, \omega_{\mu^+-i}) & \mu^+ = N+2, N+3, \ldots, 2N \end{cases}$$

The floor function of x, denoted by $\lfloor x \rfloor$, returns the greatest integer less than or equal to x; that is, $\lfloor x \rfloor = \max\{m \in \mathbb{Z} \mid m \le x\}$, where $\mathbb{Z}$ is the set of integer numbers. It is important to note that the summation extends up to $2N$ because the frequency ω_{μ^+} satisfies the condition $0 < \omega_{\mu^+} < 2\omega_{\max}$.

On the other hand, the slowly varying component for each DOF becomes:

$$F^{(-)}_{exc,2}(t) = \mathrm{Re}\left\{ \sum_{i=1}^{N} A_i A_i X^{-*}_{ii} + 2 \sum_{\mu^-=1}^{N-1} H_{\mu^-} e^{\hat{\imath}(\omega_{\mu^-})t} \right\}, \tag{13}$$

where H_{μ^-} is:

$$H_{\mu^-} = \sum_{i=1}^{N-\mu^-} A_{i+\mu^-} A^{*}_i X^{-}_i(\omega_{i+\mu^-}, \omega_i), \mu^- = 1, 2, \ldots, N-1. \tag{14}$$

The slowly varying second-order excitation force, $\mathbf{F}^{(-)}_{\text{exc},2}(t)$, can be decomposed into two parts: a *mean drift* component, associated with the diagonal terms, and a *slowly varying drift* component, arising from the off-diagonal terms. This decomposition can be written as:

$$\mathbf{F}^{(-)}_{\text{exc},2}(t) = \mathbf{F}_{\text{meanDrift}} + \mathbf{F}_{\text{slowDrift}}(t), \tag{15}$$

where the mean drift force is given by

$$\mathbf{F}_{\text{meanDrift}} = \mathrm{Re}\left(\sum_{i=1}^{N} A_i A_i X^{-*}_{ii} \right) \in \mathbb{R}, \tag{16}$$

which is a time-invariant real quantity.

Unlike the implementation of first-order excitation forces in WEC-Sim, the full-QTF approach based on Duarte's method is integrated into WEC-Sim's *body class* during the preprocessing stage. In this step, a time series vector representing the second-order excitation force is generated for each time step. During the simulation, WEC-Sim interpolates this precomputed time series to obtain the instantaneous second-order force values.

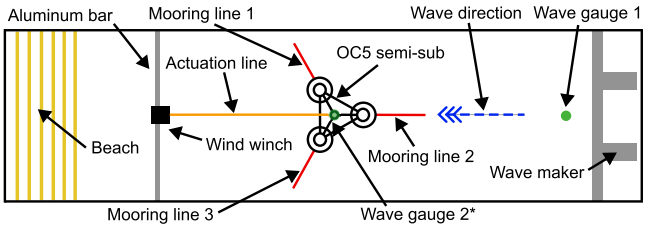

Fig. 4. Schematic of the experimental setup. Wave gauge 2 is used only during empty-tank tests, not when the model is present. Adapted from Bertozzi et al. (2025).

Table 5
Inertial properties of the model platform, reported to full scale Bertozzi et al. (2025).

Property	Value	Unit
Center of mass vertical position (w.r.t. keel)	12.29	m
Total mass	1.407×10^7	kg
Roll inertia about COG, I_{xx}	1.445×10^{10}	kg m^2
Pitch inertia about COG, I_{yy}	1.458×10^{10}	kg m^2
Yaw inertia about COG, I_{zz}	9.948×10^9	kg m^2

To account for body orientation changes, Euler angles are applied to correct the rotation of the body frame relative to its initial configuration. This method significantly improves computational efficiency, offering up to a 100× speedup compared to evaluating the convolution integral at every time step during the simulation.

4. Experimental and numerical setup

4.1. Experimental setup

The experimental campaign was carried out at Delft University of Technology using a 1:96 Froude-scaled model of the DeepCwind semi-submersible Robertson et al. (2017). Fig. 4 shows the layout of the towing tank, which measures 85 m in length and 2.75 m in width Bertozzi et al. (2024). To maintain the correct Froude scaling (full-scale water depth 100 m), the water depth was set to 1.042 m. Waves were generated by a hydraulic piston-mode wavemaker mounted on one short end of the basin; the model was positioned 28.8 m from this wavemaker. At the opposite end, a wave-absorbing beach prevented reflections. Throughout the experiments, wave propagation was aligned with the global x-axis.

Wind loading was introduced in a simplified fashion: A constant horizontal force was applied at the nacelle via a magnetic clutch attached to a transverse aluminium bar suspended above the basin. The actuation line remained parallel to the water surface to ensure consistent loading Niosi et al. (2025a).

4.1.1. Model geometry and coordinate systems

Fig. 5 presents the technical drawing of the scaled floater and its principal dimensions. The global Earth-fixed coordinate system O is located at the still-water level, centered on the undisturbed waterplane. Two body-fixed frames are defined: S, which coincides with O in the nominal (undeformed) position, and B, which is centered at the model's barycenter. Table 5 lists the full-scale inertial properties of the scaled model.

4.1.2. Mooring system

A taut mooring arrangement with three lines equally spaced at 120° was adopted. Each line comprises a long polyester segment connected to a platform fairlead and a linear spring segment linked to a load cell and anchor. Pretension was set by adjusting the polyester length using turnbuckles. The spring dominates the line stiffness, thus enabling accurate dynamic modeling Niosi et al. (2025a). Table 6 gives anchor

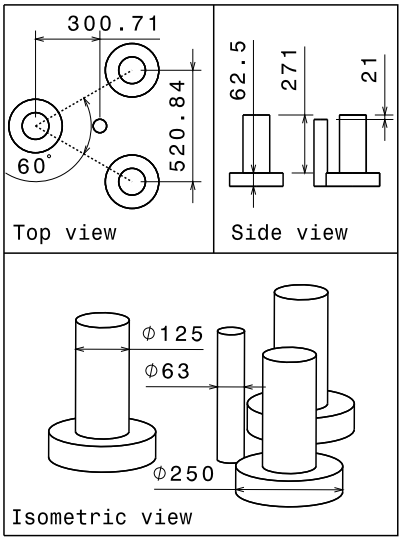

Fig. 5. Dimensions (mm and deg.) of the 1:96 scaled OC5 semi-submersible model. Adapted from Bertozzi et al. (2025).

Table 6
Anchor positions in O and fairlead positions in S, reported to full scale.

	Anchor [O]			Fairlead [S]		
Line	x (m)	y (m)	z (m)	x (m)	y (m)	z (m)
1	36.6	65.1	-100	20.4	35.4	-14
2	-75.0	0.0	-100	-40.9	0.0	-14
3	36.6	-65.1	-100	20.4	-35.4	-14

Table 7
Initial conditions and resonance periods T_r for free-decay (FD) tests (full scale).

Case	Mode	Initial Displacement	T_r (s)
FD_1	*surge*	21.22 m	98.96
FD_3	*heave*	-11.71 m	16.17
FD_5	*pitch*	-13.82°	24.59

positions in frame O and fairlead positions in frame S. Further details on the mooring design are available in Niosi et al. (2025a,b).

4.1.3. Test program

The campaign comprised free-decay tests, regular waves, and irregular sea-state experiments. Body motions were recorded by a camera-based tracking system, measuring barycentric displacements in frame O. Wave calibration runs recorded surface elevation at two gauges: gauge 2 at O (empty tank only) and gauge 1 at $x = -2$m, between the model and the wavemaker (Fig. 4).

Free-decay tests Free-decay tests determined the experimental resonant periods T_r. The identified periods, relative to *surge*, *heave*, and *pitch* motions, are summarized in Table 7. The free-decay tests are used to identify the additional viscous damping coefficients to be inserted in the numerical models, as described in Bertozzi et al. (2025).

Irregular-wave cases Twelve operational cases were generated using JONSWAP spectra, each defined by significant wave height H_s, peak period T_p, and paired wind speed W_s. Turbine thrust F_t was computed from the National Renewable Energy Laboratory (NREL) 5-MW curve Niosi et al. (2025a). Table 8 details the three cases used for validation (OP_{02}, OP_{05}, OP_{12}), all with a peak enhancement factor of 3.3 (Mediterranean conditions). An extreme-wave case (EX_{01}) was also examined in this paper (first realization only), with the turbine in parked mode (no wind load) Niosi et al. (2025a).

Table 8
Spectral parameters of irregular sea states (full scale) Niosi et al. (2025a).

Case	Description	H_s (m)	T_p (s)	W_s (m/s)	Thrust Force (kN)
OP_{02}	JONSWAP	1.37	6.17	5.0	179.5
OP_{05}	JONSWAP	1.91	6.86	11.0	690.9
OP_{12}	JONSWAP	5.62	10.30	25.0	265.5
EX_{01}	JONSWAP	8.28	12.10	N/A	N/A

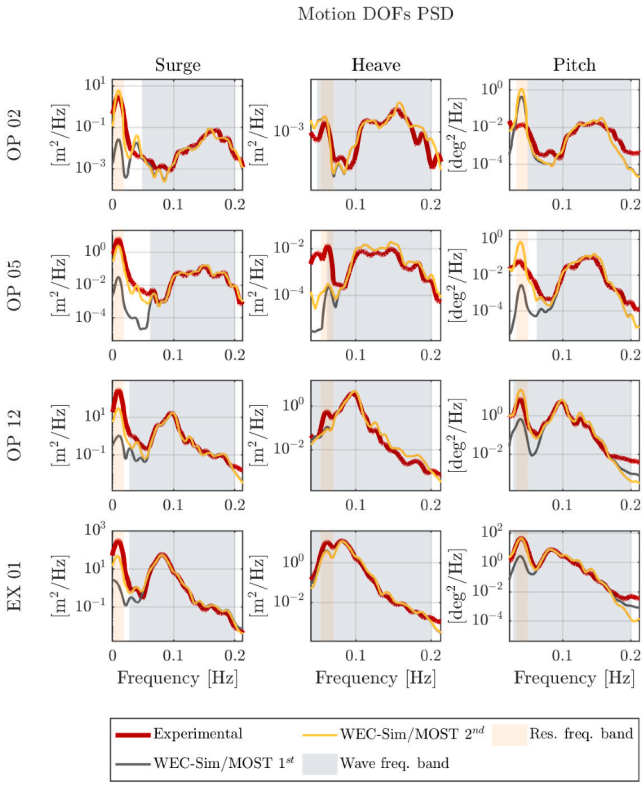

Fig. 6. Comparison between experimental and WEC-Sim/MOST (with linear or second-order wave forcing) platform motion DOFs for tests OP_{02}, OP_{05}, OP_{12}, and EX_{01}.

4.2. Numerical setup

This study validates WEC-Sim/MOST, with particular attention to the newly implemented second-order wave forcing Grasberger et al. (2025), by comparing its predictions with the full-scale-converted experimental results described in Section 4.1 and with those obtained using the established simulation tools OpenFAST and OrcaFlex. The main settings adopted in the three tools are summarized below.

- **Hydrostatics/hydrodynamics**: The hydrodynamic coefficients from the potential-flow problem were computed with the BEM solver OrcaWave, starting from the floating platform mesh. For WEC-Sim/MOST and OpenFAST, the corresponding input files were generated by converting these results; the same procedure was applied to the hydrostatic stiffness. For second-order wave forcing, the full-QTF method is applied. Displaced volume and center of buoyancy position coincide in all cases, as do the additional linear damping and quadratic drag matrices obtained from the free-decay tests (see Section 4.1.3). In every case, the wave-elevation time history measured by wave gauge 2 in the absence of the floater during the relevant experimental campaigns (OP_{02}, OP_{05}, OP_{12}, and EX_{01}; see Table 8) was used as wave input.

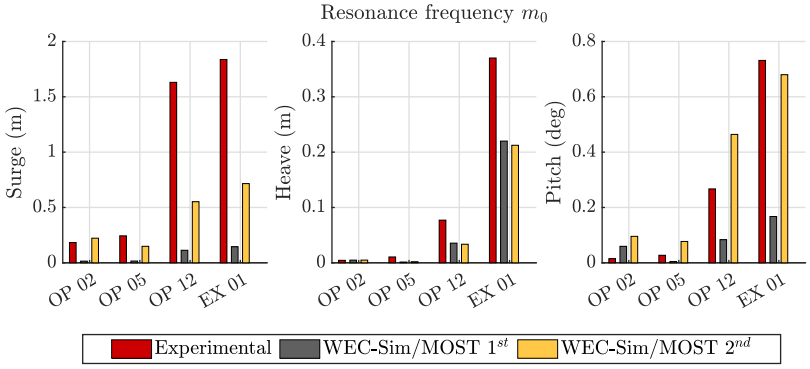

Fig. 7. Zero-order moment m_0 of *surge*, *heave*, and *pitch* PSD at resonance-frequency range for tests $OP_{02}, OP_{05}, OP_{12}$, and EX_{01}; comparison between WEC-Sim/MOST results with linear or second-order wave forcing.

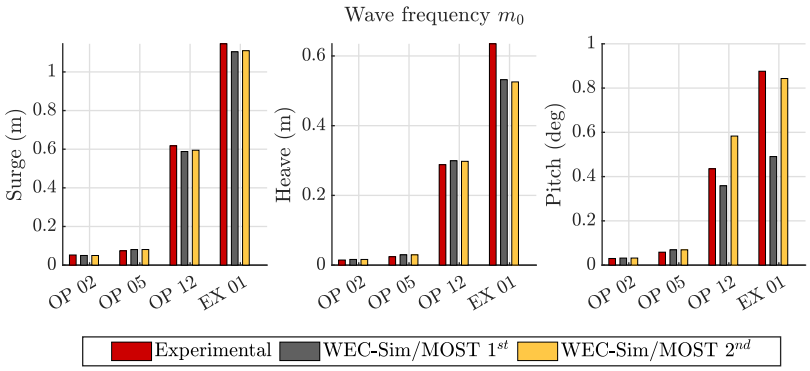

Fig. 8. Zero-order moment m_0 for *surge*, *heave*, and *pitch* PSD at wave frequency range for tests $OP_{02}, OP_{05}, OP_{12}$, and EX_{01}; comparison between WEC-Sim/MOST results with linear or second-order wave forcing.

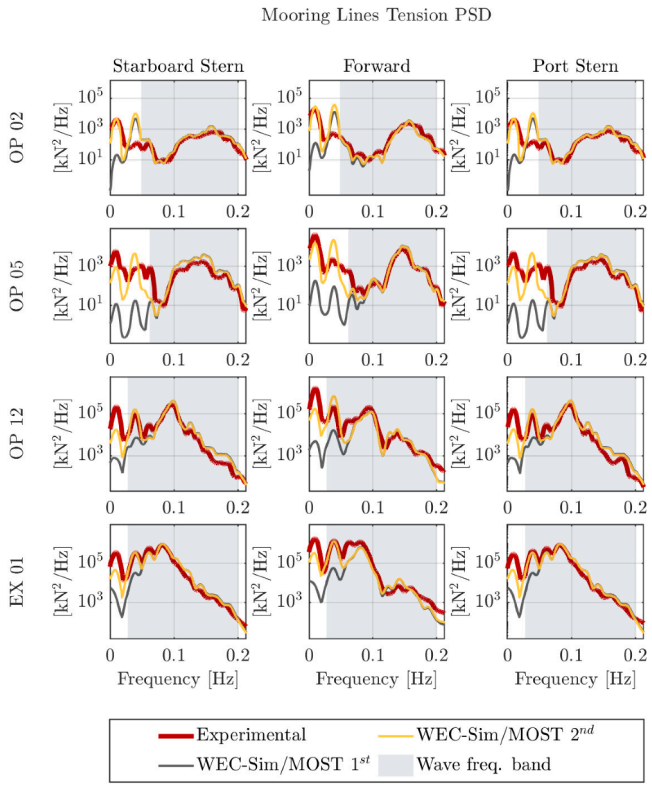

Fig. 9. Comparison between experimental and WEC-Sim/MOST (with linear or second-order wave forcing) mooring-lines tension for tests $OP_{02}, OP_{05}, OP_{12}$, and EX_{01}.

- **Body dynamics**: In all numerical models, the components are treated as rigid bodies, and the mass and inertia properties are those of the experimental setup reported in Table 5.

- **Moorings**: The mooring system corresponds to that described in Section 4.1.2. OpenFAST and WEC-Sim/MOST both employ the dedicated tool MoorDyn Moo (2020), using the same input text file; in OrcaFlex, the internal mooring module was configured with analogous characteristics.

- **Aerodynamics**: Because experimental tests were performed by applying a constant force at a given height above the water surface via a winch, the wind thrust was modeled in all three tools as a constant force, and the moment was applied at the origin of the global Earth-fixed coordinate system O. In WEC-Sim/MOST, this was implemented with appropriate Simscape Multibody blocks within the Simulink model, whereas in OpenFAST, it was introduced as an additional platform preload.

5. Results and discussions

In this section, we present the results, namely the power spectral densities (PSDs) obtained from the experimental and numerical time histories of the *surge*, *heave*, and *pitch* DOFs and of the mooring lines tension for the tests described in Section 4.1.3 ($OP_{02}, OP_{05}, OP_{12}$, and EX_{01}; see Table 8). To better quantify the deviations from the experimental results in the *surge*, *heave*, and *pitch* DOFs and mooring lines tension PSDs, we computed the zero-order moment, defined as:

$$m_0 = \sqrt{\int_{f_1}^{f_2} \mathrm{PSD}(f)\, df}, \tag{17}$$

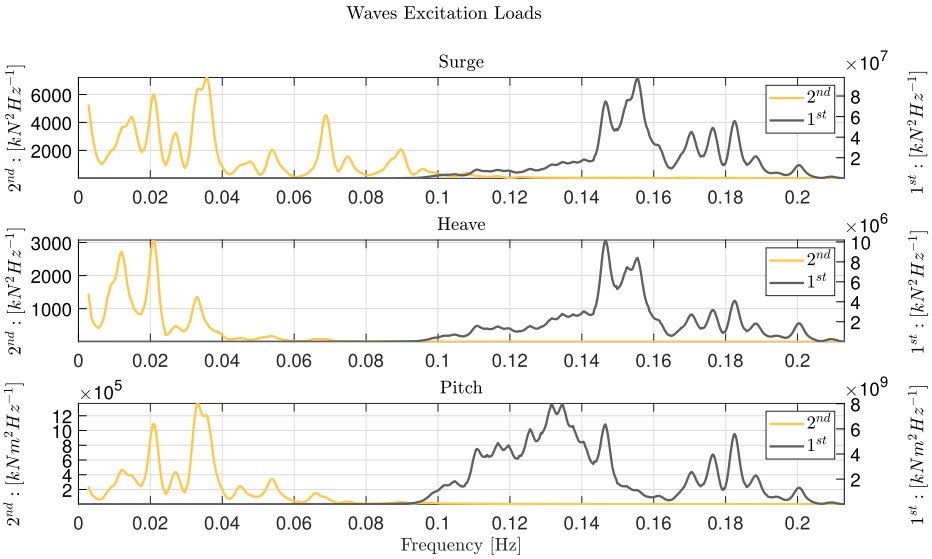

Fig. 10. Wave excitation loads (*surge*, *heave*, and *pitch*) for the OP_{05} test.

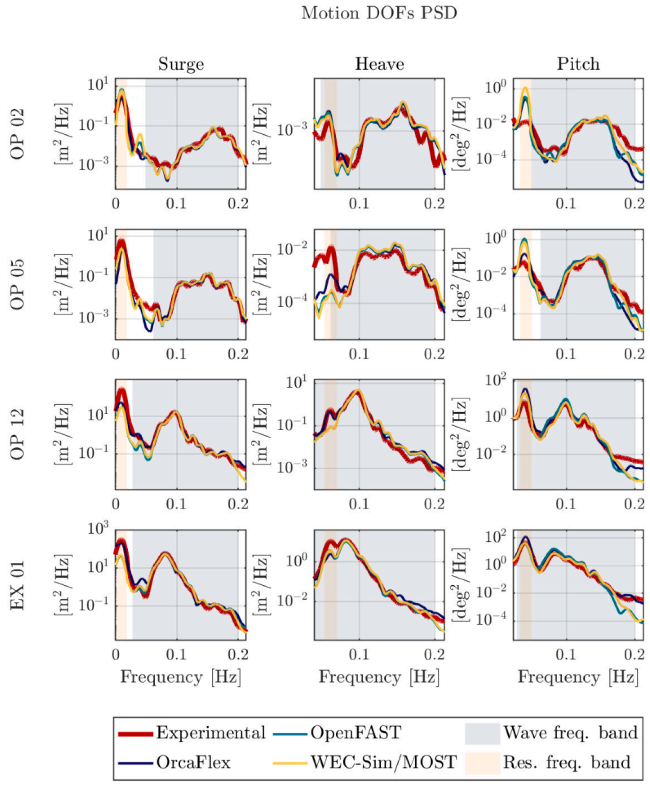

Fig. 11. Comparison between experimental, OrcaFlex, OpenFAST, and WEC-Sim/MOST platform motion DOFs for tests OP_{02}, OP_{05}, OP_{12}, and EX_{01}.

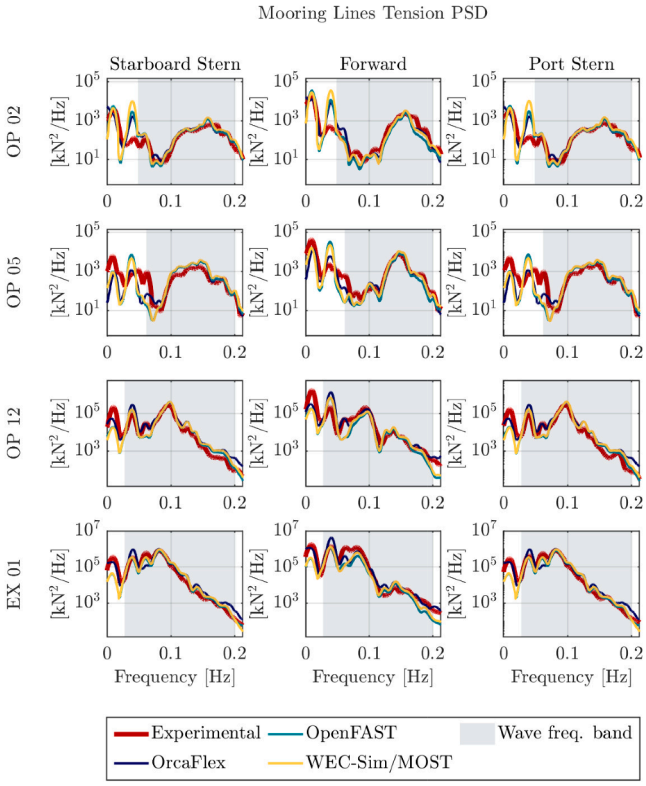

Fig. 12. Comparison between experimental, OrcaFlex, OpenFAST, and WEC-Sim/MOST mooring lines tension for tests OP_{02}, OP_{05}, OP_{12}, and EX_{01}.

where f_1 and f_2 are the integration boundaries. This parameter is evaluated over two distinct ranges: the wave frequency band, corresponding to the range in which the linear wave forcing provides a non-negligible contribution (wave freq. band, WF) and the bands around the resonance frequencies of the represented DOF (res. freq. band, RF; see Table 7) are also shown.

To isolate the contribution of nonlinear hydrodynamics, we first compare WEC-Sim/MOST simulations run with first-order forces only versus those with full-QTF second-order forces enabled (both compared with experimental results).

Fig. 6 illustrates the PSDs of *surge*, *heave*, and *pitch* motions for the tested sea states (OP_{02}, OP_{05}, OP_{12}, and EX_{01}), comparing the linear and second-order numerical solutions against experimental data.

Regarding *surge*, the figure clearly shows that the linear model fails to capture the low-frequency response. Activating the full-QTF forces recovers the slow-drift plateau, aligning the numerical prediction with physical measurements. This result is consistent with Qiao et al. Qiao et al. (2020) and Simos et al. Simos et al. (2017), who highlighted that second-order terms are mandatory to excite the resonance periods of semi-submersibles, which lie far outside the linear wave spectrum.

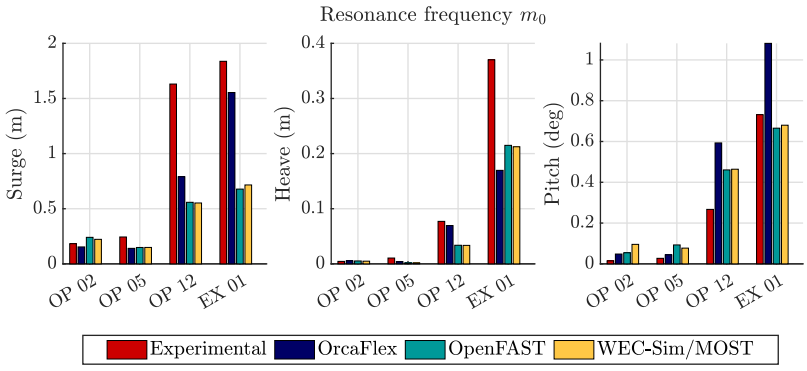

Fig. 13. Zero-order moment m_0 of *surge*, *heave*, and *pitch* PSD over the resonance-frequency range for tests OP_{02}, OP_{05}, OP_{12}, and EX_{01}; comparison between experimental, OrcaFlex, OpenFAST, and WEC-Sim/MOST.

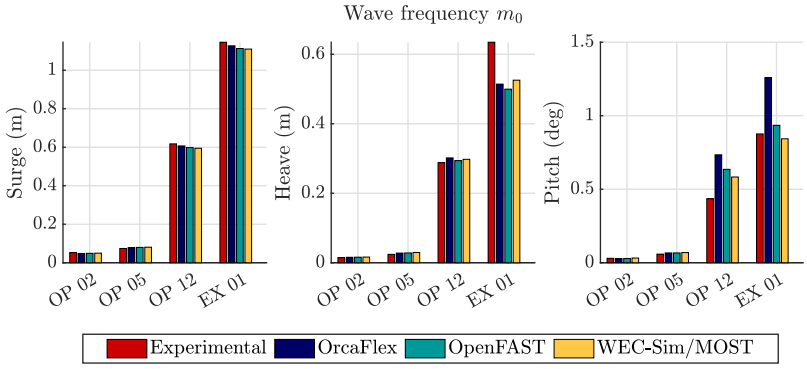

Fig. 14. Zero-order moment m_0 for *surge*, *heave*, and *pitch* PSD over the wave frequency range for tests OP_{02}, OP_{05}, OP_{12}, and EX_{01}; comparison between experimental, OrcaFlex, OpenFAST, and WEC-Sim/MOST.

For *pitch*, the impact is equally significant; while linear models underestimate the resonant response, the full-QTF implementation provides a robust prediction of pitch resonance. This corroborates the findings of Zhao et al. Zhang et al. (2020a), indicating that simplified approximations or linear models are insufficient for vertical-plane loads on shallow-draft platforms.

Regarding *heave*, a persistent underprediction of the resonant response is observed across all numerical tools (WEC-Sim/MOST, OpenFAST, and OrcaFlex), even when full second-order terms are included. As discussed by Zhang et al. Zhang et al. (2020b) and in the OC6 Phase I study Robertson et al. (2020), this limitation implies that the discrepancy is not driven by the excitation model, but rather by the modeling of hydrodynamic damping. Semi-submersibles rely on large heave plates to shift the natural period and provide damping; however, the dissipation mechanism at these plates is dominated by flow separation and vortex shedding at the sharp edges. This viscous damping is inherently nonlinear and strongly dependent on the oscillation amplitude and the Keulegan-Carpenter number. The calibration procedure adopted Bertozzi et al. (2025), while rigorous for decay tests, yields a set of constant coefficients tuned on specific decay amplitudes. In irregular sea states, the stochastic interaction between wave orbital velocities and body motion creates a state-dependent damping regime that a constant coefficient model cannot fully capture. To fully resolve this a more sophisticated sea-state-dependent calibration of the drag coefficients should be applied.

This analysis is quantified by the m_0 moments shown in Fig. 7 (RF) and Fig. 8 (WF): while the wave frequency energy is well captured by both linear and second-order models, the resonance energy in surge and pitch is almost entirely missing in the linear formulation and is substantially recovered by the full-QTF implementation.

The impact on the mooring system is shown in Fig. 9, which presents the mooring lines tension PSDs. The tension response reflects the dynamics of the surge motion. The linear model severely underpredicts the low-frequency tension cycles, which are critical for fatigue life. The full-QTF model successfully reconstructs the tension spectrum in the resonance band, confirming its necessity for accurate station-keeping design Niosi et al. (2025a).

The excitation load spectra for OP_{05} in Fig. 10 elucidate the underlying physical mechanism. First-order wave excitation is strictly confined to the wave frequency lobe (prominent content at $\sim$ 0.14 - 0.2 Hz). In contrast, the difference-frequency second-order excitation is broad-banded and populates the low-frequency range ($<$ 0.1 Hz). Although the magnitude of these second-order forces is significantly smaller than the first-order peaks (note the different scales in the figure), their spectral placement is critical: they deposit energy directly into the platform's natural frequency range where the hydrodynamic radiation damping is vanishingly small. This explains why the linear model, which lacks this low-frequency forcing mechanism, appears "blind" to the resonant dynamics, resulting in the flat response observed in Fig. 6.

Having established the necessity of the full-QTF formulation, we now benchmark the complete WEC-Sim/MOST model against OpenFAST and OrcaFlex (all compared with experimental results). Fig. 11 (motions) and Fig. 12 (tensions) illustrate the PSD comparisons across all tested sea states.

In the wave frequency band, all three numerical tools show good agreement with each other and with the experimental data. This confirms that the linear solution is consistently implemented across the different solvers. Deviations emerge primarily in the resonance frequency band. Fig. 13 (RF) and Fig. 14 (WF) provide the quantitative comparison of the zero-order moments m_0 between the codes.

OrcaFlex generally exhibits the closest match to experimental peaks in the low-frequency range, likely because of the way second-order forces are computed: at each integration step, the instantaneous vessel position is used to update the phase of every wave component, and

Table 9
Simulation run times for the considered test cases.

Case	Simulated	OrcaFlex	OpenFAST	WEC-Sim/MOST
OP_{02}	3680 s	294400 s	2684 s	1441 s
OP_{05}	3917 s	313360 s	2997 s	1506 s
OP_{12}	3548 s	283840 s	2551 s	1350 s
EX_{01}	3100 s	248000 s	2021 s	1146 s

the complete double summation over the full-QTF matrix must be recomputed to obtain the corresponding drift and sum-frequency loads. In contrast, both OpenFAST and WEC-Sim/MOST pre-compute the time histories of the second-order wave forces assuming a fixed reference position of the body, then apply these pre-evaluated loads to the displaced vessel during the dynamic simulation. WEC-Sim/MOST and OpenFAST, probably because of the less accurate calculation method, show a slight underestimation in the resonance energy in the most severe sea states (OP_{12}, EX_{01}) compared to the higher fidelity commercial benchmark.

Finally, Table 9 highlights the computational efficiency of the implemented approach. WEC-Sim/MOST achieves simulation times approximately two orders of magnitude faster than the high-fidelity commercial solver OrcaFlex for the same analysis. This speedup is primarily due to the pre-computation strategy employed for the second-order forces, as opposed to the instantaneous re-computation at each time step.

6. Conclusions

This work implemented full sum- and difference-frequency QTFs in WEC-Sim/MOST and validated the resulting solver against a 1:96 Froude-scaled DeepCwind semi-submersible Robertson et al. (2017), with a code-to-code comparison to OpenFAST and OrcaFlex across operational and extreme seas. Overall, promising results are obtained regarding the comparison between experimental and numerical tests. However, it should be emphasized that the experimental benchmark is based on a scaled model, and therefore the similarity of the Reynolds number is not preserved. Consequently, the relative contribution of viscous damping and low-frequency response may differ on a real scale, so extrapolation to the real scale of the calibrated resistance terms must be carried out with caution. In the future, it will be beneficial to extend the same methodology to larger-scale and/or real-scale data sets, when available.

Focusing more on the results obtained, the solver reproduces the expected spectral structure of platform motions and mooring tensions. On the wave frequency band, the three tools exhibit close agreement with the experiments for *surge* and *heave* and only modest deviations for *pitch*. On the low/resonance band, enabling full-QTFs is necessary to recover slow-drift energy in *surge* and, to a lesser extent, in *pitch*, and to reproduce the resonance band plateau of the mooring lines tension. In the all-codes comparison, OrcaFlex is generally closest to experiments. These outcomes are consistent with the established understanding that second-order loads are essential for semi-submersible slow-drift dynamics.

Present conclusions align with and extend prior findings on the OC4/DeepCwind system. Bayati et al. Bayati et al. (2014) and Qiao et al. Qiao et al. (2020) demonstrated that difference-frequency effects are required to reproduce measured slow-drift responses, while Zhao et al. Zhang et al. (2020a) emphasized the importance of second-order loads for vertical plane motions. The OC6 Phase IV blind study Bergua et al. (2024) further showed that models neglecting second-order kinematics systematically under-predict resonance frequency motions and tensions. The present campaign confirms these points for WEC-Sim/MOST and quantifies the benefits of explicit QTF inclusion in an open, mid-fidelity framework, with direct, like-for-like benchmarking against widely used reference tools.

Remaining mismatches at the most severe seas, notably the underprediction of *heave* at resonance, highlight the challenge of modeling amplitude-dependent viscous damping. Although the employed two-stage calibration method Bertozzi et al. (2025) effectively identifies linear and quadratic coefficients from decay tests, these constant parameters do not fully capture the complex, state-dependent viscous damping that occurs in irregular wave fields. Future work should therefore focus on implementing automated routines for the sea-state-dependent calibration of drag coefficients. Despite this, the inclusion of second-order drift forces is shown to be non-negotiable for the accurate estimation of mooring loads. Neglecting these terms would lead to a severe underestimation of the tension cycles and, consequently, of the Damage Equivalent Load (DEL) for fatigue analysis, potentially compromising the safety factors of the station-keeping system.

With all input decks and source code released under GPL-3.0, WEC-Sim/MOST offers an open, transparent environment that meets the IEC 61400-3-2 requirements on nonlinear load inclusion. The tool retains a computational speed advantage of approximately two orders of magnitude over industry-standard engineering tools like OrcaFlex for the cases analyzed. While the pre-computation of QTF forces introduces a mild approximation regarding the instantaneous wetted surface, the agreement in results suggests that this trade-off is acceptable for engineering design. This efficiency effectively fills the gap identified by Fadaei et al. Fadaei et al. (2024) for mid-fidelity tools, enabling computationally intensive workflows such as Monte Carlo simulations for reliability analysis or algorithm-based optimization of floater geometry.

CRediT authorship contribution statement

Davide Issoglio: Writing – review & editing, Writing – original draft, Visualization, Validation, Software, Resources, Project administration, Methodology, Formal analysis, Data curation, Conceptualization; **Mohamed A. Shabara:** Writing – review & editing, Writing – original draft, Visualization, Validation, Software, Resources, Methodology, Investigation, Formal analysis; **Ermando Petracca:** Writing – review & editing, Writing – original draft, Visualization, Validation, Software, Resources, Methodology, Formal analysis, Data curation, Conceptualization; **Francesco Niosi:** Writing – review & editing, Writing – original draft, Visualization, Validation, Software, Methodology, Investigation, Formal analysis, Data curation, Conceptualization; **Adam Keester:** Writing – review & editing, Writing – original draft, Visualization, Validation, Supervision, Methodology, Investigation, Funding acquisition, Formal analysis, Data curation, Conceptualization; **Massimo Sirigu:** Writing – review & editing, Visualization, Validation, Software, Methodology, Conceptualization; **Giovanni Bracco:** Writing – review & editing, Visualization, Validation, Supervision, Project administration, Funding acquisition, Conceptualization.

Data availability

The datasets generated and/or analyzed during the current study are available from the corresponding author on reasonable request.

Declaration of competing interest

The authors declare that they have no known competing financial interests or personal relationships that could have appeared to influence the work reported in this paper.

Acknowledgement

This research was conducted within the Ph.D. Program in Mechanical Engineering (XXXIX Cycle) at Politecnico di Torino. The Ph.D. position is funded by the Ministry of University and Research (MUR), under Ministerial Decree n. 118 of 2023 (Investment I.4.1 PNRR Public Administration Scholarships), utilizing resources from the National Recovery and Resilience Plan (PNRR). The associated Unique Project Code (CUP)

is: E14D23001800006. This work was authored in part by National Laboratory of the Rockies (NLR) for the U.S. Department of Energy (DOE), operated under Contract No. DE-AC36-08GO28308. Funding provided by the U.S. Department of Energy Office of Energy Efficiency and Renewable Energy Water Power Technologies Office. The views expressed in the article do not necessarily represent the views of the DOE or the U.S. Government. The U.S. Government retains and the publisher, by accepting the article for publication, acknowledges that the U.S. Government retains a nonexclusive, paid-up, irrevocable, worldwide license to publish or reproduce the published form of this work, or allow others to do so, for U.S. Government purposes. Sandia National Laboratories is a multimission laboratory managed and operated by National Technology & Engineering Solutions of Sandia, LLC, a wholly owned subsidiary of Honeywell International Inc., for the U.S. Department of Energy's National Nuclear Security Administration under contract DE-NA0003525. This paper describes objective technical results and analysis. Any subjective views or opinions that might be expressed in the paper do not necessarily represent the views of the U.S. Department of Energy or the United States Government.

References

Abbas, N. J., Zalkind, D. S., Pao, L., Wright, A., 2022a. A reference open-source controller for fixed and floating offshore wind turbines. Wind Energy Sci. 7 (1), 53–73. https://doi.org/10.5194/wes-7-53-2022

Abbas, N. J., Zalkind, D. S., Pao, L. Y., Wright, A. D., 2022b. A reference open-source controller for fixed and floating offshore wind turbines. Wind Energy Sci. 7 (1), 53–73. https://doi.org/10.5194/wes-7-53-2022

Bai, H., Zhang, J., Ma, G., Sun, K., Kang, W.-H., Lai, Y., Chen, Y., Zhu, R., 2025. Structural modeling and optimization design of 15MW semi-submersible floating wind turbine platform based on intelligent algorithms. Energy 335, 137947. https://doi.org/10.1016/j.energy.2025.137947.

Bayati, I., Jonkman, J., Robertson, A., Platt, A., 2014. Effects of second-order hydrodynamics on a semisubmersible floating offshore wind turbine: preprint. National Renewable Energy Laboratory (NREL), Golden, CO., 524. https://doi.org/10.1088/1742-6596/524/1/012094

Bergua, R., Wiley, W., Robertson, A., Jonkman, J., Brun, C., et al., 2024. Oc6 project phase iv: validation of numerical models for novel floating offshore wind support structures. Wind Energy Sci. 9, 1025–1051. https://doi.org/10.5194/wes-9-1025-2024

Bertozzi, A., Niosi, F., Dell'Edera, O., Paduano, B., Bracco, G., 2025. Innovative calibration procedure of numerical models for FOWTs: an experimental validation. In: Proceedings of the EERA DeepWind Conference. Trondheim, Norway. Paper accepted and in production.

Bertozzi, A., Niosi, F., Jiang, X., Jiang, Z., 2024. Numerical calibration of the mooring system for a semi-submersible floating wind turbine model. J. Offshore Mech. Arct. Eng. 146 (6). https://doi.org/10.1115/1.4065551

Bureau Veritas, 2019. Classification and Certification of Floating Offshore Wind Turbines. Technical Report, Bureau Veritas, Technical guidance document.

Carmo, L., Hall, M., 2025. Slender-body approach for computing second-order wave loads in the frequency domain. Ocean Eng. 322, 120558. https://doi.org/10.1016/j.oceaneng.2025.120558

Coulling, A.J., Goupee, A.J., Robertson, A.N., Jonkman, J.M., 2013. Importance of second-Order difference-Frequency wave-Diffraction forces in the validation of a FAST semi-Submersible floating wind turbine model. Ocean Renewable Energy of International Conference on Offshore Mechanics and Arctic Engineering 8, https://doi.org/10.1115/OMAE2013-10308

Cummins, W. E., 1962. The Impulse Response Function and Ship Motions. Technical Report. David Taylor Model Basin.

Duarte, T., Sarmento, A., Jonkman, J., 2014. Effects of second-order hydrodynamic forces on floating offshore wind turbines. In: AIAA SciTech 2014, pp. 1–16. https://doi.org/10.2514/6.2014-0361

Dnvgl-rp-c205 2017, Environmental conditions and environmental loads, edition august 2017, https://www.dnv.com/energy/standards-guidelines/dnv-rp-c205-environmental-conditions-and-environmental-loads/.

Fadaei, P., Afagh, F., Langlois, R., 2024. A survey of numerical simulation tools for offshore wind turbine systems. Renew. Sustain. Energy Rev. 185, 113714. https://doi.org/10.3390/wind4010001

Fontanella, A., Al, M., van Wingerden, J.-W., Belloli, M., 2021. Model-based design of a wave-feedforward control strategy in floating wind turbines. Wind Energy Sci. 6 (3), 885 – 901. Cited by: 19; All Open Access, Gold Open Access, Green Open Access. https://doi.org/10.5194/wes-6-885-2021.

Grasberger, J., Shabara, M., Keester, A., Ruehl, K., Forbush, D., Husain, S., Leon, J., Ogden, D., Davies, R., 2025. Review of recent WEC-sim (v6. 1) advanced features. Int. Mar. Energy J. 8 (3), 259–263.

Hall, M., 2020. Moordyn V2: new capabilities in mooring system components and load cases. Ocean Renewable Energy of International Conference on Offshore Mechanics and Arctic Engineering. 9 https://doi.org/10.1115/OMAE2020-19341

Hansen, M. H., Hansen, A., Larsen, T., Øye, S., Sørensen, P., Fuglsang, P., 2005. Control design for a pitch-regulated, variable speed wind turbine. no. 1500(EN) In Denmark. Forskningscenter Risoe. Risoe-R.

Huang, S., Tang, X., Wang, K., Zhou, F., 2025. Fully coupled time domain dynamic analyses and actual sea state experimental validation of a multi-body floating wave energy converter. Energy 321, 135133. https://doi.org/10.1016/j.energy.2025.135133

International Electrotechnical Commission (IEC), 2025, IEC 61400-3-2:2025 — Wind Energy generation systems — Part 3-2: design requirements for floating offshore wind turbines, https://webstore.iec.ch/en/publication/67761.

Jonkman, B., Platt, A., Mudafort, R. M., Branlard, E., Sprague, M., Ross, H., Slaughter, D., jjonkman, J., HaymanConsulting, cortadocodes, Hall, M., Vijayakumar, G., Buhl, M., Russell9798, Bortolotti, P., Davies, R., Crozier, R., Ananthan, S., Michael, S., psakievich, 2024. OpenFAST/openfast: v4.0.0 (v4.0.0). https://doi.org/{{10.5281/zenodo.14553563}}.

Larsen, T. J., Hansen, A. M., 2025. How 2 HAWC2: the User's manual. Roskilde, Denmark.

Mei, X., Xiong, M., 2021. Effects of second-order hydrodynamics on the dynamic responses and fatigue damage of a 15 MW floating offshore wind turbine. J. Mar. Sci. Eng. 9 (11). https://doi.org/10.3390/jmse9111232

Morison, J. R., Johnson, J. W., Schaaf, S. A., 1950. The force exerted by surface waves on piles. J. Petrol. Technol. 2 (05), 149–154. https://doi.org/10.2118/950149-G

Ning, A., Hayman, G., Damiani, R., Jonkman, J. M., 2026. Development and Validation of a New Blade Element Momentum Skewed-Wake Model within AeroDyn. https://doi.org/10.2514/6.2015-0215

Ning, S. A., 2014. A simple solution method for the blade element momentum equations with guaranteed convergence. Wind Energy 17 (9), 1327–1345. https://doi.org/10.1002/we.1636

Niosi, F., Dell'edera, O., Glorioso, M., Paduano, B., Giorgi, G., Schreier, S., 2025a. Experimental investigation and dataset release of a taut-leg mooring system for a semi-submersible floating offshore wind turbine. Ocean Eng. 328. https://doi.org/10.1016/j.oceaneng.2025.121067

Niosi, F., Dell'Edera, O., Paduano, B., Giorgi, G., Schreier, S., 2025b. Experimental investigation of taut leg moored FOWTs in damaged conditions. In: Innovation in Renewable Energy Offshore - Proceedings of the 6Th International Conference on Renewable Energies Offshore (RENEW 2024, 19–21 November 2024, Lisbon, Portugal).

Orcina, L., 2023. OrcaFlex Documentation, Version 11.4. https://www.orcina.com/SoftwareProducts/OrcaFlex/.

Pinkster, J., 1980. Low frequency second order wave exciting forces on floating structures.

Qiao, D., Yan, J., Li, W., Ning, D., 2020. Coupled dynamic analysis of a floating offshore wind turbine with a semi-submersible platform. Renew. Energy 157, 644–660. https://doi.org/10.1016/j.renene.2020.05.039

Repi, V., Diputra, A., 2022. Simulation and validation of floating-point absorber (FPA) wave energy converter (WEC) using open-source WEC-sim simulation. AIP Publishing, Online. https://doi.org/10.1063/5.0108138

Robertson, A. N., Gueydon, S., Bachynski, E., Wang, L., Jonkman, J., et al., 2020. Oc6 phase i: investigating the underprediction of low-frequency hydrodynamic loads and responses of a floating wind turbine. J. Phys. Conf. Ser. 1618 (3), 032033. NREL report version available: https://doi.org/10.1088/1742-6596/1618/3/032033

Robertson, A. N., Wendt, F., Jonkman, J. M., Popko, W., Dagher, H., Gueydon, S., Qvist, J., Vittori, F., Azcona, J., Uzunoglu, E., Soares, C. G., Harries, R., Yde, A., Galinos, C., Hermans, K., de Vaal, J. B., Bozonnet, P., Bouy, L., Bayati, I., Bergua, R., Galvan, J., Mendikoa, I., Sanchez, C. B., Shin, H., Oh, S., Molins, C., Debruyne, Y., 2017. Oc5 project phase ii: validation of global loads of the deepcwind floating semisubmersible wind turbine. Energy Procedia 137, 38–57. https://doi.org/10.1016/j.egypro.2017.10.333

Ruehl, K., Michelen, C., Yu, Y., Lawson, M., 2016. Update on WEC-sim validation testing and code development. METS, Washington D.C., USA.

Standing, R.G., Brendling, W.J., Wilson, D., 1987. Recent developments in the analysis of wave drift forces, low-Frequency damping and response, vol. offshore technology conference of OTC offshore technology conference. https://doi.org/10.4043/5456-MS

Simos, A., Ruggeri, F., Watai, R., Souto-Iglesias, A., Lopez-Pavon, C., 2017. Slow-drift of a floating wind turbine: an assessment of frequency-domain methods based on model tests. Renew. Energy 116. https://doi.org/10.1016/j.renene.2017.09.059

Skaare, B., Nielsen, F. G., Hanson, T. D., Yttervik, R., Havmøller, O., Rekdal, A., 2015. Analysis of measurements and simulations from the hywind demo floating wind turbine. Wind Energy 18 (6), 1105–1122. https://doi.org/10.1002/we.1750

Stewart, G., Muskulus, M., 2016. A review and comparison of floating offshore wind turbine model experiments. Energy Procedia 94, 227–231. 13th Deep Sea Offshore Wind R&D Conference, EERA DeepWind 2016. https://doi.org/10.1016/j.egypro.2016.09.228

Voltá i Roqueta, L., Thomas, S., Schmidt Paulsen, U., 2020. Modelling of a wind-wave floating and semi-submersible power plant. In: Journal of Physics: Conference Series. https://doi.org/10.1088/1742-6596/1618/5/052032

WAMIT, I., 2012. Wamit user manual,versions 7.0. https://www.wamit.com/manualupdate/history/V70_Manual.pdf.

Wang, L., Robertson, A., Jonkman, J., Liao, Y., Berthelsen, P. A., Abdelmoteleb, S.-E., Rohrer, P., Vishnu, 2025. Oc7 phase i: toward practical sea-state-dependent modeling of hydrodynamic viscous drag and damping. Ocean Eng. 336, 121745. https://doi.org/10.1016/j.oceaneng.2025.121745

WEC-Sim Documentation, 2025. Advanced features: Quadratic transfer function import. https://wec-sim.github.io/WEC-Sim/.

Yang, J., He, Y.-P., Zhao, Y.-S., Shao, Y.-L., Han, Z.-L., 2021. Experimental and numerical studies on the low-frequency responses of a spar-type floating offshore wind turbine. Ocean Eng. 222, 108571. https://doi.org/10.1016/j.oceaneng.2021.108571

Zhang, L., Shi, W., Karimirad, M., Michailides, C., Jiang, Z., 2020a. Second-order hydrodynamic effects on the response of three semisubmersible floating offshore wind turbines. Ocean Eng. 207, 107371. https://doi.org/10.1016/j.oceaneng.2020.107371

Zhang, Y., Hu, Z., Ng, C., 2020b. Dynamic response of a 10 MW floating wind turbine with a concrete semi-submersible foundation. Renew. Energy 162, 2231–2247. https://doi.org/10.1016/j.renene.2020.10.027